

RL-TR-96-283
Final Technical Report
April 1997



HOLOGRAPHIC PROCESSING OF HIGH-SPEED LIGHTWAVE SIGNALS FOR THE TIME-DIVISION MULTIPLEXING

Purdue University

Andrew M. Weiner, David D. Nolte, and M.R. Melloch

APPROVED FOR PUBLIC RELEASE; DISTRIBUTION UNLIMITED.

DTIC QUALITY INSPECTED 4

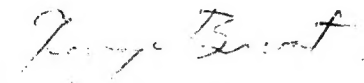
**Rome Laboratory
Air Force Materiel Command
Rome, New York**

19970715 212

This report has been reviewed by the Rome Laboratory Public Affairs Office (PA) and is releasable to the National Technical Information Service (NTIS). At NTIS it will be releasable to the general public, including foreign nations.

RL-TR-96-283 has been reviewed and is approved for publication.

APPROVED:



GEORGE A. BROST
Project Engineer

FOR THE COMMANDER:



GARY D. BARMORE, Major, USAF
Deputy Director
Surveillance & Photonics Directorate

If your address has changed or if you wish to be removed from the Rome Laboratory mailing list, or if the addressee is no longer employed by your organization, please notify RL/OCPA, 25 Electronic Pky, Rome, NY 13441-4514. This will assist us in maintaining a current mailing list.

Do not return copies of this report unless contractual obligations or notices on a specific document require that it be returned.

REPORT DOCUMENTATION PAGE			Form Approved OMB No. 0704-0188	
Public reporting burden for this collection of information is estimated to average 1 hour per response, including the time for reviewing instructions, searching existing data sources, gathering and maintaining the data needed, and completing and reviewing the collection of information. Send comments regarding this burden estimate or any other aspect of this collection of information, including suggestions for reducing this burden, to Washington Headquarters Services, Directorate for Information Operations and Reports, 1215 Jefferson Davis Highway, Suite 1204, Arlington, VA 22202-4302, and to the Office of Management and Budget, Paperwork Reduction Project (0704-0188), Washington, DC 20503.				
1. AGENCY USE ONLY (Leave blank)		2. REPORT DATE April 1997		3. REPORT TYPE AND DATES COVERED FINAL, Jul 95 - Jul 96
4. TITLE AND SUBTITLE HOLOGRAPHIC PROCESSING OF HIGH-SPEED LIGHTWAVE SIGNALS FOR THE TIME-DIVISION MULTIPLEXING			5. FUNDING NUMBERS C - F30602-95-C-0137 PE - 62702F PR - 4600 TA - P4 WU - PU	
6. AUTHOR(S) Andrew M. Weiner, David D. Nolte, M.R. Melloch				
7. PERFORMING ORGANIZATION NAME(S) AND ADDRESS(ES) Purdue University School of Electrical and Computer Engineering and Department of Physics West Lafayette IN 47907-1396			8. PERFORMING ORGANIZATION REPORT NUMBER N/A	
9. SPONSORING / MONITORING AGENCY NAME(S) AND ADDRESS(ES) Rome Laboratory/OCPA 25 Electronic Pky Rome NY 13441-4515			10. SPONSORING / MONITORING AGENCY REPORT NUMBER RL-TR-96-283	
11. SUPPLEMENTARY NOTES Rome Laboratory Project Engineer: George A. Brost, OCPA, (315) 330-7669				
12a. DISTRIBUTION AVAILABILITY STATEMENT Approved for Public Release; Distribution Unlimited			12b. DISTRIBUTION CODE	
13. ABSTRACT (Maximum 200 words) Photorefractive quantum well devices were evaluated for use in holographic processing of high-speed lightwave signals by measuring the shape of a diffracted femtosecond pulse. Pulses diffracted from photorefractive quantum wells were broadened, but remained nearly transform limited. The phase of the diffracted pulse remained essentially flat.				
14. SUBJECT TERMS photorefraction, multiple quantum wells, short pulse, holographic processing			15. NUMBER OF PAGES 36	
			16. PRICE CODE	
17. SECURITY CLASSIFICATION OF REPORT UNCLASSIFIED	18. SECURITY CLASSIFICATION OF THIS PAGE UNCLASSIFIED	19. SECURITY CLASSIFICATION OF ABSTRACT UNCLASSIFIED	20. LIMITATION OF ABSTRACT UNLIMITED	

TABLE OF CONTENTS

I. Introduction	1
II. Femtosecond Pulses and Photorefractive Multiple Quantum Wells	2
III. Pulse Shape Measurements.....	6
IV. Experiment	10
V. Data and Analysis.....	14
VI. References.....	26

LIST OF FIGURES

Fig. 1. Experimental geometry for diffracting pulses from the photorefractive quantum wells.	6
Fig. 2. Optical properties of the photorefractive quantum wells.....	12
Fig. 3. Calculated diffraction spectra of the photorefractive quantum wells.	13
Fig. 4. Reference pulse auto-correlation vs. delay.....	15
Fig. 5. Gaussian fits to reference pulse.	16
Fig. 6. Electric field autocorrelation of reference pulse and inverse Fourier transform of reference pulse power spectrum.....	17
Fig. 7. Cross-correlation of transmitted pulse with reference pulse.	18
Fig. 8. Spectrum of transmitted pulse.	19
Fig. 9. Spectrum of transmitted pulse and calculated spectrum.	20
Fig. 10. Electric field cross-correlation of transmitted pulse.	20
Fig. 11. Electric field cross-correlation of the diffracted pulse and the reference pulse.....	22
Fig. 12. Spectra of the diffracted pulse.	23
Fig. 13. Spectrum of the diffracted pulse compared with calculation.	24
Fig. 14. Electric-field cross correlation of diffracted pulse with reference pulse.	25

HOLOGRAPHIC PROCESSING OF HIGH-SPEED LIGHTWAVE SIGNALS FOR THE TIME-DIVISION MULTIPLEXING

I. Introduction

Ultrafast pulses contain a wide bandwidth, with 4 THz for a typical 100 fs pulse duration, or 10 nm at a center wavelength of 850 nm (~ 20 nm at a center wavelength of 1550 nm). The successful use of this bandwidth is desirable for high throughput of coded data in fiber optic communications channels. One method to achieve this is to combine N parallel channels each with bandwidth B into one channel with bandwidth NB , such as through wavelength division multiplexing, with the total bandwidth divided into N frequency intervals that are each modulated independently over the bandwidth B . Another method is time division multiplexing, with the modulation over the entire bandwidth using N time intervals, one for each input channel. Unfortunately, no modulator is available that can operate at 4 THz. One technique to shape ultrafast pulses over their full bandwidth is to use a Fourier-domain pulse shaper to manipulate the pulse in the frequency domain to obtain the desired pulse characteristics [1]. This technique has been extensively demonstrated for fixed Fourier masks [2] and programmable liquid crystal modulator Fourier masks with phase control [3] and amplitude and phase control [4]. Placement of a holographic material in the Fourier plane enables more complex and nonlinear operations, such as reversal of a pulse in time [5]. For dynamic pulse shaping, an ideal diffraction material has flat amplitude *and* phase response over the bandwidth of the pulses, and a fast response time for high repetition rates. Photorefractive quantum wells are a candidate for the dynamic holographic medium in a pulse shaper [6, 7]. Diffraction from quantum wells relies on absorption and index gratings with strong wavelength dependence. The chief question investigated in this research is whether these strong dispersion effects significantly distort the ultrafast pulse. Photorefractive quantum wells are evaluated for use in a pulse shaper by measuring the shape of a diffracted femtosecond pulse.

Previous work in bulk photorefractive crystals with two-wave mixing of femtosecond pulses includes pulse characterization [8, 9] and pulse shaping [10, 11]. Bulk ferroelectric materials have the advantage of large photorefractive response, but the disadvantage of long grating formation times. Also, two-wave mixing is trivially phase-matched, but four-wave mixing requires tedious Bragg matching of a third beam in bulk materials. Short pulses can also suffer from broadening by dispersion when traversing a long interaction length in a bulk crystal. In contrast, photorefractive multiple quantum wells have a short grating formation time, and thin film diffraction allows four-wave mixing without a Bragg condition. Quantum wells can also be engineered in several material systems.

In the nondegenerate four-wave mixing geometry described here, femtosecond pulses diffract from a grating written by an above-gap CW diode laser. This is in contrast to previous work with photorefractive quantum wells where a near gap CW diode laser beam diffracts from a grating written by above-gap femtosecond pulses to find the electric-field correlation function. This was accomplished both with direct interference [12], and interference in a Fourier-transform joint correlator geometry (time-to-space mapping) [13]. In both cases, photorefractive quantum wells are used to characterize the shape of femtosecond pulses, but not change their shape, by obtaining the square of the electric-field correlation envelope. The conceptual power of time-to-space mapping is the correspondence to spatial image processing techniques. These techniques are exploited in spectral holography.

In the following section II presents the theory of diffraction of femtosecond pulses from photorefractive quantum wells and section III describes measurement of pulse shapes by two different interferometric techniques, electric-field cross correlation and spectral interferometry. Section IV describes the photorefractive quantum well optical properties and the experimental procedures, and Section V, data and analysis.

II. Femtosecond Pulses and Photorefractive Multiple Quantum Wells

In this section, the temporal shape of a femtosecond pulse will be theoretically calculated for pulses transmitted through and diffracted from a photorefractive quantum well. The most convenient method is to Fourier transform the input pulse into the frequency domain. The transmission or diffraction of a pulse is represented by a filter function, which is multiplied by the input electric field and then inverse Fourier transformed to obtain the temporal shape of the output pulse.

Femtosecond pulses are emitted from a modelocked laser in a train with repetition time T_{REP} , and a pulse duration is given as the full-width half-maximum (FWHM) t_p . The center frequency is ω_c , the center wavelength is $\lambda_c = 2\pi c/\omega_c$, the propagation vector is \vec{k} and the unit propagation vector is \hat{k} . The electric field for one pulse is

$$\vec{e}(\vec{x}, t) = \hat{e} E_0 f(t - \hat{k} \cdot \vec{x} / c) \exp \left(i \left(\vec{k} \cdot \vec{x} - \omega_c t \right) \right) \quad (1)$$

where \hat{e} is the polarization vector, E_0 is the electric field amplitude, and $f(t)$ is the pulse shape function. Note the sign convention in the exponential. In what follows, the polarization and position are known and fixed, so the polarization vector is dropped, and \vec{x} is set to 0. The electric field simplifies to

$$e(t) = E_0 f(t) \exp(-i\omega_c t) \quad (2)$$

and the intensity is

$$I(t) = \frac{1}{2Z} |e(t)|^2 = I_{AVG} T_{REP} |f(t)|^2 \quad (3)$$

where Z is the wave impedance, and the normalization of the pulse shape function is chosen to be

$$\int_{-\infty}^{\infty} |f(t)|^2 dt = 1 \quad (4)$$

so that

$$\frac{1}{T_{REP}} \int_{-\infty}^{\infty} I(t) dt = I_{AVG} \quad (5)$$

The function $f(t)$ is typically a hyperbolic secant or a gaussian function for modelocked pulses. For a gaussian,

$$f(t) \propto \exp \left(-2 \ln 2 \left(\frac{t}{t_p} \right)^2 \right) \quad (6)$$

where t_p is the FWHM duration.

Transformations between the time and frequency domains are accomplished with the Fourier transforms

$$\begin{aligned} E(\omega) &= F\{e(t)\} = \int_{-\infty}^{\infty} e(t) \exp(i\omega t) dt \\ e(t) &= F^{-1}\{E(\omega)\} = \frac{1}{2\pi} \int_{-\infty}^{\infty} E(\omega) \exp(-i\omega t) d\omega \end{aligned} \quad (7)$$

$$e(t) \xleftrightarrow{\text{Fourier}} E(\omega)$$

which, for gaussian pulses, yields the relationships

$$\begin{aligned} I(t) &\propto \exp \left(-4 \ln 2 \left(\frac{t}{t_p} \right)^2 \right) & |E(\omega)|^2 &\propto \exp \left(-\frac{1}{4 \ln 2} \left(t_p (\omega - \omega_c) \right)^2 \right) \\ \downarrow \uparrow & & \downarrow \uparrow & \\ e(t) &\propto \exp \left(-2 \ln 2 \left(\frac{t}{t_p} \right)^2 - i\omega_c t \right) & \xleftrightarrow{\text{Fourier}} & E(\omega) \propto \exp \left(-\frac{1}{8 \ln 2} \left(t_p (\omega - \omega_c) \right)^2 \right) \end{aligned} \quad (8)$$

The time bandwidth product for a gaussian is $t_p \Delta \nu = t_p 4 \ln 2 / 2\pi t_p = 2 \ln 2 / \pi \approx 0.441$. If a varying phase is added to the pulse, the pulse may become distorted. Generally, the phase can be expanded in a power series of the frequency. The constant term is trivial. The linear term is also trivial, since it only causes a shift in the conjugate variable. The lowest nontrivial term is the quadratic term, which causes chirp. There may also be higher order terms. Chirp may be caused by dispersion of a pulse transmitted through a material. In this case, the relationships are

$$\begin{aligned} I(t) &\propto \exp \left(-4 \ln 2 \left(\frac{t}{t_p} \right)^2 \right) & |E(\omega)|^2 &\propto \exp \left(-\frac{1}{4 \ln 2} \left(\frac{t_p (\omega - \omega_c)}{\sqrt{1 + \beta^2}} \right)^2 \right) \\ \downarrow \uparrow & & \downarrow \uparrow & \\ e(t) &\propto \exp \left(-2 \ln 2 (1 + i\beta) \left(\frac{t}{t_p} \right)^2 - i\omega_c t \right) & \xleftrightarrow{\text{Fourier}} & E(\omega) \propto \exp \left(-\frac{1}{8 \ln 2} (1 - i\beta) \left(\frac{t_p (\omega - \omega_c)}{\sqrt{1 + \beta^2}} \right)^2 \right) \end{aligned} \quad (9)$$

where β is a parameter characterizing the amount of chirp. The sign of β is chosen so that $\beta > 0$ corresponds to positive chirp (low frequencies ahead of high frequencies), and normal dispersion ($dn/d\omega > 0$). If the chirp is caused by dispersion, then the bandwidth remains constant, that is $t_p / \sqrt{1 + \beta^2}$ is constant, so larger dispersion results in a longer pulse duration. The time bandwidth product for a chirped gaussian pulse is $t_p \Delta\nu = 2\ln 2 \sqrt{1 + \beta^2} / \pi$. Transform limited pulses are the shortest possible pulse for a given power spectrum. Therefore, increasing dispersion causes longer pulses.

The transmission or diffraction of a pulse can be represented by a complex filter function $H(\omega)$ in the frequency domain. For transmission,

$$E_T(\omega) = E_{IN}(\omega) H_T(\omega) . \quad (10)$$

Neglecting Fresnel reflection at the surfaces of the thin film and the associated Fabry-Perot effects, the filter function for transmission is

$$H_T(\omega) = \exp \left(i \tilde{n}(\omega) k L \right) \quad (11)$$

where $\tilde{n}(\omega) = n(\omega) + i\alpha(\omega) / 2k$ is the complex refractive index, k is the propagation constant in free space, and L is the sample thickness. The transmission spectrum is

$$T(\omega) = |H_T(\omega)|^2 = \exp \left(- \alpha(\omega) L \right), \quad (12)$$

which can be measured.

In nondegenerate four-wave mixing, femtosecond pulses diffract from a grating written in the semiconductor thin-film by a CW laser with a photon energy above the bandgap of the semiconductor, as shown in Fig. 1. Photorefractive quantum wells operate by the photogeneration, transport and trapping of charge at deep level defects, and an electro-optic effect. The interference of the two writing beams creates a periodic intensity pattern $I(x)$ which induces a refractive index pattern

$$\tilde{n}(x, \omega) = \tilde{n}(\omega) + \Delta \tilde{n}(\omega) f(Kx + \phi) \quad (13)$$

through the photorefractive effect, where $\Delta \tilde{n}(\omega) = \Delta n(\omega) + i\Delta\alpha(\omega) / 2k$ is the complex change in refractive index caused by the electro-optic effect, which implicitly depends on the applied electric field as well as beam ratio, fringe spacing, and material parameters involving transport. The grating vector is K , and ϕ is the phase offset between the intensity pattern and the index pattern. The function $f(Kx + \phi)$ is a periodic function with period 2π , and is generally not a sinusoid due to the nonlinearities in the transport and the electro-optic effect. The writing beams completely determine the refractive index in Eq. 13, where the frequency ω is for the probe beam. The spectral dependence in Eq 13 is determined by the transmission and electro-optic spectra of the thin-film structure. The photon energy of the writing beams is implicitly included in K .

In the thin grating limit, the spatially varying phase shift diffracts the incident pulse into many orders without requiring phase-matching. The strongest diffraction is from the lowest

harmonic (fundamental) grating, so $f(Kx + \phi)$ is taken to be $\cos(Kx + \phi)$ [14]. The total electric-field at the exit face of the material is

$$E_{ALL}(\omega) = E_{IN}(\omega) \exp \left(i \tilde{n}(\omega) kL \right) \exp \left(\Delta \tilde{n}(\omega) kL \cos (Kx + \phi) \right). \quad (14)$$

Using the relation

$$\exp \left(iz \cos (\delta) \right) = \sum_{m=-\infty}^{\infty} i^m J_m(z) \exp (im\delta) \quad (15)$$

and the previous definition for $H_T(\omega)$,

$$E_{ALL}(\omega) = E_{IN}(\omega) H_T(\omega) \sum_{m=-\infty}^{\infty} i^m J_m \left(\Delta \tilde{n}(\omega) kL \right) \exp \left(im(Kx + \phi) \right) \quad (16)$$

which contains all diffracted orders. The first-order diffracted electric-field is for $m = 1$,

$$E_D(\omega) = E_{IN}(\omega) H_T(\omega) i J_1 \left(\Delta \tilde{n}(\omega) kL \right) \exp \left(i(Kx + \phi) \right). \quad (17)$$

Using the approximation $J_m(z) \approx z^m / 2^m m!$ for small z , and neglecting the phases, which are unimportant, the electric field is written in terms of a filter function $E_D(\omega) = E_{IN}(\omega) H_D(\omega)$, where

$$\begin{aligned} H_D(\omega) &= H_T(\omega) \frac{1}{2} \left(\Delta \tilde{n}(\omega) kL \right) \\ &= H_T(\omega) \frac{1}{2} \left(\Delta n(\omega) kL + i \Delta \alpha(\omega) \frac{L}{2} \right) \end{aligned} \quad (18)$$

and the power spectrum for the diffracted pulse is

$$\begin{aligned} |E_D(\omega)|^2 &= |E_{IN}(\omega)|^2 |H_D(\omega)|^2 \\ &= |E_{IN}(\omega)|^2 |H_T(\omega)|^2 \frac{1}{4} \left| \Delta n(\omega) kL + i \Delta \alpha(\omega) \frac{L}{2} \right|^2 \\ &= |E_{IN}(\omega)|^2 T(\omega) \frac{1}{4} \left[\left(\Delta n(\omega) kL \right)^2 + \left(\Delta \alpha(\omega) \frac{L}{2} \right)^2 \right] \end{aligned} \quad (19)$$

and the input diffraction efficiency is $\eta_{IN}(\omega) = |E_D(\omega)|^2 / |E_{IN}(\omega)|^2 = |H_D(\omega)|^2$ and the output diffraction efficiency is $\eta_{OUT}(\omega) = |E_D(\omega)|^2 / |E_T(\omega)|^2 = |H_D(\omega)|^2 / |H_T(\omega)|^2$.

In the time domain, the electric field is $e_D(t) = F^{-1}\{E_D(\omega)\}$. The shape of the pulse is $I_D(t) = |e_D(t)|^2 / 2Z$. Unfortunately, it is difficult to directly measure the temporal profile of an ultrashort pulse. Therefore, several indirect techniques must be used, including linear electric-field interference of the signal pulse with a reference pulse, and nonlinear correlation of the intensity

profile with a reference pulse. With a known reference pulse, the signal pulse can be fully characterized.

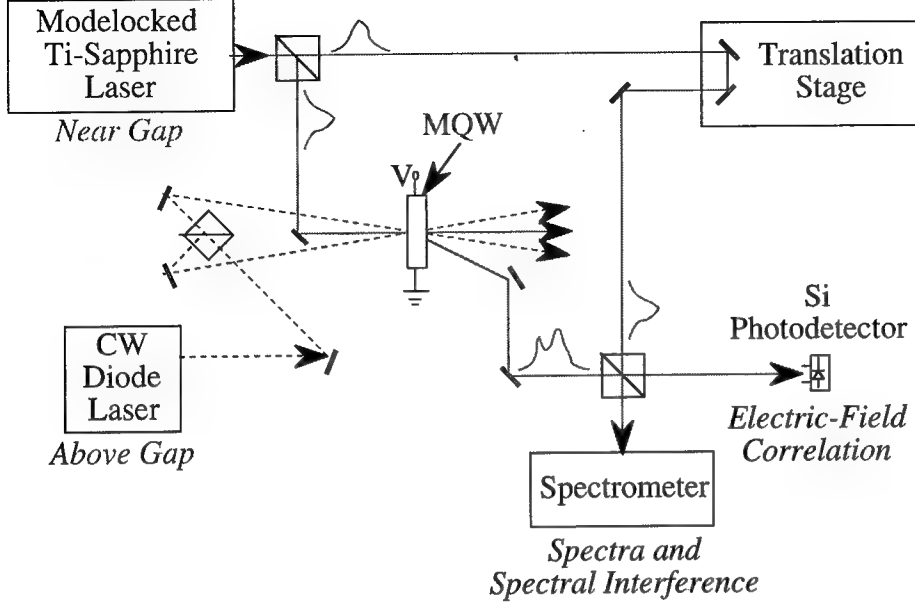


Fig. 1. Experimental geometry for diffracting pulses from the photorefractive quantum wells. The shape of the diffracted pulses is inferred from electric-field cross-correlation as well as spectral and spectral interferometry methods. An above-gap CW diode laser writes the grating for nondegenerate four-wave mixing. The CW beam is shown as the dashed line.

III. Pulse Shape Measurements

Three linear techniques can be used to determine the shape of the diffracted pulse, as shown in Fig. 1. These techniques include finding the electric-field cross-correlation of the diffracted pulses with the reference pulse, finding the spectra of the diffracted and reference pulses, and finding the spectral interference of the diffracted pulse and the reference pulse. The interference of the signal pulse (the transmitted pulse or the diffracted pulse) and the reference pulse (the input pulse) result in a total electric field

$$E_{TOTAL}(t, \tau) = E_S(t) + E_R(t - \tau) \quad (20)$$

$$= E_S f_S(t) \exp(-i\omega_S t) + E_R f_R(t - \tau) \exp(-i\omega_R(t - \tau))$$

where τ is the delay of the reference pulse relative to the signal pulse. The reference pulse is the input pulse, and the intensity of the interference is

$$I_{TOTAL}(t, \tau) = \frac{1}{2Z} |E_{TOTAL}(t, \tau)|^2 \quad (21)$$

$$= \frac{1}{2Z} |E_S(t)|^2 + \frac{1}{2Z} |E_R(t - \tau)|^2 + \frac{1}{Z} \text{Re} \left(E_S(t) E_R^*(t - \tau) \right)$$

$$= I_S(t) + I_R(t - \tau) + 2\sqrt{I_S I_R} \text{Re} \left(f_S(t) f_R^*(t - \tau) \exp(-i\Delta\omega t) \exp(-i\omega_c \tau) \right)$$

where $\Delta\omega = \omega_S - \omega_R$. In the following, the frequency difference is incorporated into f_S , and $\Delta\omega = 0$. A standard silicon photodetector cannot respond faster than 10 ns, which is much longer than 100 fs. Therefore, the detected intensity is averaged

$$\begin{aligned}
I_{TOTAL}(\tau) &= \int_{-\infty}^{\infty} I_{TOTAL}(t, \tau) dt \\
&= I_S + I_R + 2\sqrt{I_S I_R} \operatorname{Re} \left(\exp(-i\omega_c \tau) \int_{-\infty}^{\infty} f_S(t) f_R^*(t - \tau) dt \right) \\
&= I_{TOTAL} \left(1 + m \operatorname{Re} \left(\exp(-i\omega_c \tau) \gamma_{S,R}(\tau) \right) \right) \\
&= I_{TOTAL} \left(1 + m |\gamma_{S,R}(\tau)| \cos \left(\arg(\gamma_{S,R}(\tau)) - \omega_c \tau \right) \right)
\end{aligned} \tag{22}$$

where $m = 2\sqrt{I_S I_R} / (I_S + I_R)$ is the modulation depth of the interference, and

$$\gamma_{S,R}(\tau) = \int_{-\infty}^{\infty} f_S(t) f_R^*(t - \tau) dt \tag{23}$$

is the correlation function, which contains all the useful information about the interference. For a gaussian signal and a gaussian reference pulse, when both are transform limited,

$$|\gamma_{S,R}(\tau)| \propto \exp \left(-4 \ln 2 \frac{\tau^2}{2(t_S^2 + t_R^2)} \right) \tag{24}$$

which has a width $\tau_{S,R} = \sqrt{2(t_S^2 + t_R^2)}$, and reduces to $\tau_{R,R} = 2t_R$ for an autocorrelation. The correlation function can also be found for the case where the signal pulse is a chirped gaussian, but the analytic expression is complicated, and therefore not directly useful. Generally, the width of the correlation will be smaller than expected for a transform limited pulse of the same duration, due to the reduced coherence between the signal and reference pulses. In the special case where signal is a chirped gaussian with the same power spectrum as the reference, the duration of the signal pulse is $t_S = t_R \sqrt{1 + \beta^2}$ and the correlation width is $\tau_{S,R} = 2t_R \sqrt{1 + (\beta/2)^2}$. This is the case where the pulse is transmitted through a transparent material with dispersion.

A connection between the time domain and the frequency domain can be made through the Fourier transform of the correlation function

$$\gamma_{S,R}(\tau) \xLeftrightarrow{\text{Fourier}} F_S(\omega) F_R^*(\omega) \tag{25}$$

and in the case of autocorrelation reduces to

$$\gamma_{R,R}(\tau) \xLeftrightarrow{\text{Fourier}} |F_R(\omega)|^2 \propto |E_R(\omega)|^2 \tag{26}$$

which is just the power spectrum. This is useful for checking consistency between time domain electric-field autocorrelation and the power spectrum.

In the frequency domain, there is interference of the spectra [15, 16]. Following Ref. [16], the electric-field in the frequency domain is

$$\begin{aligned} E_{TOTAL}(\omega, \tau) &= E_S(\omega) + E_R(\omega) \exp(i\omega\tau) \\ &= E_S F_S(\omega - \omega_R) + E_R F_R(\omega - \omega_R) \exp(i\omega\tau) \end{aligned} \quad (27)$$

and the detected intensity from spectral inteferometry is

$$\begin{aligned} |E_{TOTAL}(\omega, \tau)|^2 &= |E_S(\omega)|^2 + |E_R(\omega) \exp(i\omega\tau)|^2 \\ &\quad + 2\text{Re} \left(E_S(\omega) E_R^*(\omega) \exp(-i\omega\tau) \right) \\ &= |E_S(\omega)|^2 + |E_R(\omega)|^2 + 2|E_S(\omega)| |E_R(\omega)| \cos(\Delta\phi_{S,R}(\omega) - \omega\tau) \end{aligned} \quad (28)$$

where $\Delta\phi_{S,R}(\omega) = \arg(E_S(\omega)) - \arg(E_R(\omega)) = \arg(F_S(\omega - \omega_R)) - \arg(F_R(\omega - \omega_R))$ is the phase of the signal spectrum relative to the phase of the reference spectrum. The interference may seem counterintuitive, because there is interference even when the pulses are separated by a delay much greater than the pulse length. However, since the maximum delay is inversely proportional to the resolution of the spectrometer, a particular wavelength interval is effectively spread in time to a shape that is the inverse Fourier transform of the spectrometer bandpass function. Therefore, a resolution that is ten times smaller than the pulse bandwidth will allow spectral interference when the pulses are separated by as much as $10t_p$. An equivalent viewpoint is that the delay must be short enough for the spectrometer to resolve the interference fringes. If the maximum delay is exceeded, the fringes are washed out so that the measured quantity is the sum of the individual power spectra.

The spectral interference contains both individual spectra as well as the interference. The individual spectra are each measured separately and subtracted from the interference to obtain the interference spectrum

$$\begin{aligned} S(\omega, \tau) &= |E_{TOTAL}(\omega, \tau)|^2 - |E_S(\omega)|^2 - |E_R(\omega)|^2 \\ &= 2\text{Re} \left(E_S(\omega) E_R^*(\omega) \exp(-i\omega\tau) \right) \\ &= 2 E_S E_R \text{Re} \left(F_S(\omega - \omega_R) F_R^*(\omega - \omega_R) \exp(-i\omega\tau) \right) \end{aligned} \quad (29)$$

which has a functional form similar to the correlation function, i.e., a pulse function on a carrier or an envelope with oscillations. Also, both the correlation and the spectral interferometry data are real parts of a complex function. To calculate the envelope magnitude and the phase of the oscillations, one can recover the complex function from the real function. For a function $x(t)$ (such as the electric field correlation),

$$\begin{aligned}
x(\tau) &= 2\text{Re} \left(\tilde{x}(\tau) \exp(-i\omega_c \tau) \right) \\
&= \tilde{x}(\tau) \exp(-i\omega_c \tau) + \tilde{x}^*(\tau) \exp(i\omega_c \tau) \\
F\{x(\tau)\} &= \tilde{X}(\omega - \omega_c) + \tilde{X}^*(-\omega - \omega_c) \\
\theta(\omega)F\{x(\tau)\} &= \tilde{X}(\omega - \omega_c) \\
F^{-1}\{\theta(\omega)F\{x(\tau)\}\} &= \tilde{x}(\tau) \exp(-i\omega_c \tau)
\end{aligned} \tag{30}$$

where $\theta(\omega)$ is the step function that selects the positive frequency values. For a function $X(\omega)$ (such as the spectral interference),

$$\begin{aligned}
X(\omega) &= 2\text{Re} \left(\tilde{X}(\omega) \exp(i\omega \tau) \right) \\
&= \tilde{X}(\omega) \exp(i\omega \tau) + \tilde{X}^*(\omega) \exp(-i\omega \tau) \\
F^{-1}\{X(\omega)\} &= \tilde{x}(t - \tau) + \tilde{x}^*(-t - \tau) \\
\theta(t)F^{-1}\{X(\omega)\} &= \tilde{x}(t - \tau) \\
F\{\theta(t)F^{-1}\{X(\omega)\}\} &= \tilde{X}(\omega) \exp(i\omega \tau)
\end{aligned} \tag{31}$$

In both cases, the transform of the real function is the sum of the desired function shifted to the right and its complex conjugate shifted to the left. The overall operation is valid when the function and its conjugate do not overlap at the origin, so that the step function selects all of the desired function and none of its conjugate. For the electric-field cross-correlation using Eq. 30, the condition is that the bandwidth of the pulse is much smaller than the center frequency. This is equivalent to a slowly varying envelope approximation where there are many oscillations under the envelope of the function. This is true for 100 fs pulses in the infrared, but breaks down for 10 fs pulses. Similarly, for the spectral interference using Eq. 31, the condition is that the delay must be much larger than the pulse width, again so that there are many oscillations under the envelope. In this case, the delay can be chosen to satisfy this condition.

Both interferometric techniques depend on the characteristics of the reference pulse. Spectral interference of two pulses provides the relative phase of the pulses. If the reference pulse is close to transform limited, the phase difference is the phase of the signal pulse. The combination of second-harmonic autocorrelation and measurement of the spectrum of the reference pulse can be used to estimate how close the pulse is to transform limited. When the reference pulse is not transform limited, a technique such as frequency resolved optical gating (FROG) [17] must be used to fully characterize the reference pulse. Standard techniques are sufficient for this work because the reference pulses are assumed to be well behaved and the frequency difference between the signal pulse and the reference pulse is the quantity of interest.

Second harmonic generation correlation depends on the intensity of the pulse. For background free second harmonic correlation, the second harmonic output intensity is

$$\begin{aligned}
I_{2\omega}^{BF}(\tau) &= \langle I_{2\omega}(t, \tau) \rangle \\
&= \langle I_S(t) I_R(t - \tau) \rangle
\end{aligned} \tag{32}$$

where $\langle \rangle$ denotes time average over a repetition period. The interferometric second harmonic generation correlation depends on the relative phase of the two pulses. If the amplitudes are taken to be equal, the second harmonic intensity (using the total electric field from Eq. 20) is

$$\begin{aligned}
I_{2\omega}^{INT}(\tau) &= \langle I_{2\omega}(t, \tau) \rangle \\
&\propto \langle |E_{2\omega}(t, \tau)|^2 \rangle \\
&\propto \langle |E_{TOTAL}^2(t, \tau)|^2 \rangle \\
&\propto \left\langle |f_S(t)|^4 + |f_R(t - \tau)|^4 + 4|f_S(t)|^2 |f_R(t - \tau)|^2 \right. \\
&\quad + f_S^2(t) f_R^{*2}(t - \tau) \exp(-2i\omega_c \tau) \\
&\quad + 2f_S^2(t) f_S^*(t) f_R^*(t - \tau) \exp(-i\omega_c \tau) \\
&\quad \left. + 2f_S(t) f_R(t - \tau) f_R^{*2}(t - \tau) \exp(-i\omega_c \tau) \right\rangle
\end{aligned} \tag{33}$$

The measured intensity at the peak is eight times the value for large pulse separations. When the interferometric intensity is averaged over one interference fringe,

$$\begin{aligned}
\omega_c \int_0^{\omega_c^{-1}} I_{2\omega}^{INT}(\tau - \tau') d\tau' &= \left\langle |f_S(t)|^4 + |f_R(t - \tau)|^4 + 4|f_S(t)|^2 |f_R(t - \tau)|^2 \right\rangle \\
&= I_S^2 + I_R^2 + 4I_{2\omega}^{BF}(\tau)
\end{aligned} \tag{34}$$

which is the background free result with a background due to the second harmonic of each pulse. For gaussian pulses,

$$I_{2\omega}^{BF}(\tau) \propto \exp\left(-4\ln 2 \frac{\tau^2}{t_S^2 + t_R^2}\right) \tag{35}$$

which has a width of $\tau_{S,R}^{BF} = \sqrt{t_S^2 + t_R^2}$, and reduces to $\tau_{R,R}^{BF} = \sqrt{2} t_R$ for autocorrelation.

IV. Experiment

The multiple quantum well structure used in our experiment was grown by molecular beam epitaxy in a Varian Gen II chamber. The growth began with 0.5 μm GaAs on a semi-insulating GaAs substrate, followed by 500 nm of $\text{Al}_{0.5}\text{Ga}_{0.5}\text{As}$, 20 nm of AlAs, and 10 nm of GaAs was grown for substrate removal etches. After 250 nm of $\text{Al}_{0.1}\text{Ga}_{0.9}\text{As}$, 85 periods of 7.5 nm GaAs wells and 10 nm of $\text{Al}_{0.1}\text{Ga}_{0.9}\text{As}$ barriers were deposited, followed by 150 nm of $\text{Al}_{0.1}\text{Ga}_{0.9}\text{As}$.

After growth, the samples were proton implanted with a dose of 10^{12} cm^{-2} at 160 keV and $5 \times 10^{11} \text{ cm}^{-2}$ at 80 keV to create deep level defects and render the material semi-insulating [18, 19] and photorefractive [6, 20]. The implanted wafer was cleaved into 3 mm x 3 mm pieces. To remove the substrate for transmission experiments, the substrate was lapped to 100 μm , and then etched with a 1:19 ammonium hydroxide/hydrogen peroxide etch to the 50% Al stop etch layer [21]. Then an HF acid etch removed the 50% Al layer and the AlAs layer [22]. Gold contacts are evaporated directly onto the low bandgap GaAs layer with a 1 mm aperture across which a field is applied in the plane of the quantum wells, perpendicular to the growth direction.

The transmission and electro-optic effect of the photorefractive quantum wells are shown in Fig. 2. The data are measured using a 1000 W halogen source filtered by a 0.85 m double spectrometer. There is a peak absorption due to the quantum-confined heavy-hole exciton of approximately 10^4 cm^{-1} for the 1.9 μm thickness of the quantum well region. The change in absorption and the change in the refractive index spectra due to the electro-optic effect are shown in Fig. 2(b). The electro-optic effect with a field applied in the plane of the quantum wells is due to the field ionization of the excitons, which broadens both the light-hole exciton absorption feature and the heavy-hole absorption feature, resulting in a characteristic double dip. The differential transmission is measured by applying a sinusoid that varies between 0 V and 400 V with a frequency of 277 Hz. The change in absorption is calculated using

$$\Delta\alpha(F, \lambda) = -\frac{1}{L} \ln \left(\frac{\Delta T(F, \lambda)}{T(\lambda)} + 1 \right) \quad (36)$$

where L is the thickness and F is the applied field. The change in refractive index was calculated using the Kramers-Kronig transformation

$$\Delta n(\omega) = \frac{c}{\pi} \mathcal{P} \int_0^\infty \frac{\Delta\alpha(s)}{s^2 - \omega^2} ds \quad (37)$$

with a maximum absorption change of 1000 cm^{-1} and a maximum refractive index change of 0.005. The CW input diffraction efficiency spectrum shown in Fig. 3(a) is calculated directly from the transmission and electro-optic spectra using Eq. 19. Since the heavy-hole exciton oscillator strength is much larger than light-hole exciton oscillator strength, the peak is almost entirely due to the heavy hole exciton, with a maximum input diffraction efficiency of 10^{-4} . The spectrum of the diffracted phase shown in Fig. 3(b) is calculated only from the changes in absorption and refractive index, and not from the background index spectrum, which is not known in detail. Despite the oscillation in the electro-optic spectrum, the phase is relatively flat. That is, the change in refractive index spectrum is approximately the same as for the change in absorption, but shifted by a constant phase, because of the relationship through the Kramers-Kronig transform.

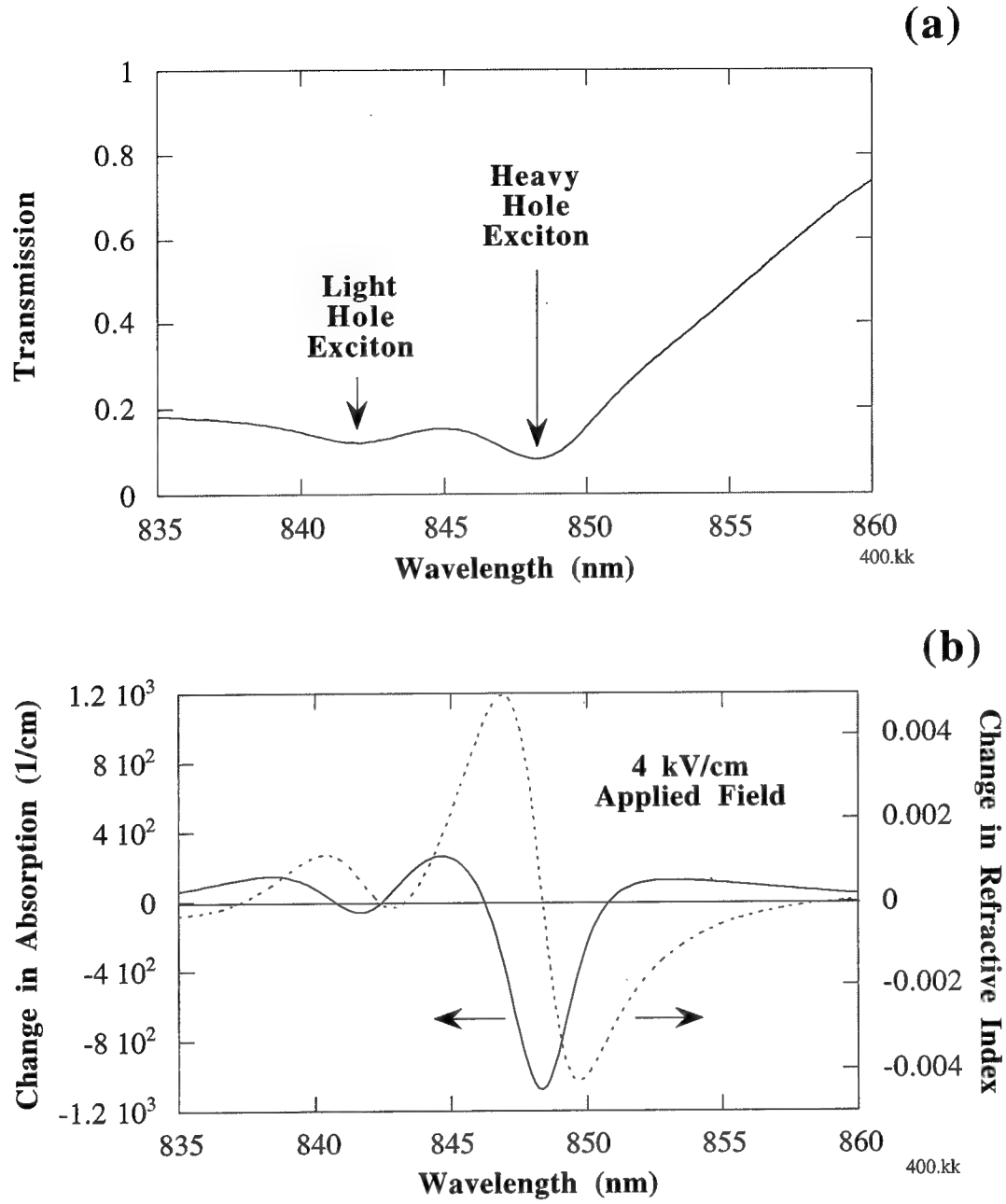


Fig. 2. Optical properties of the photorefractive quantum wells: (a) transmission spectrum; (b) spectra for change in absorption and change in refractive index due to electro-optic effect, with 4 kV/cm applied field. The refractive index change is calculated from the change in absorption using the Kramers-Kronig transform.

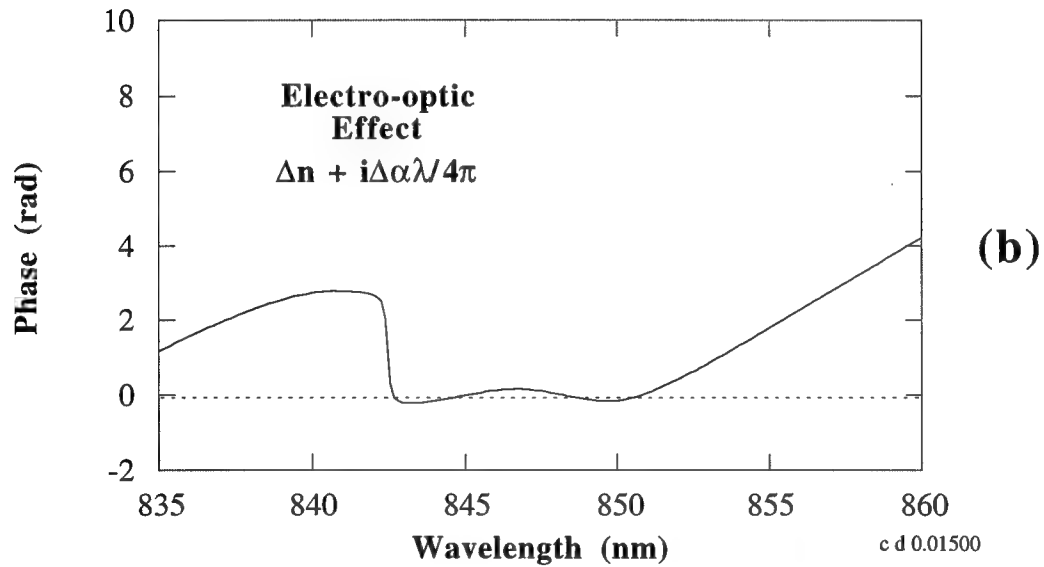
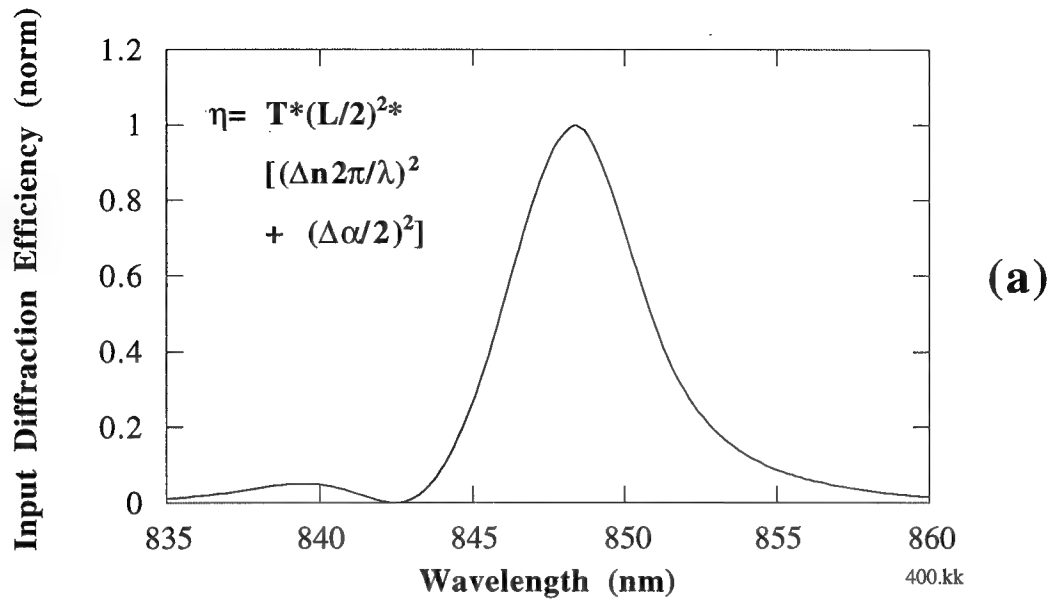


Fig. 3. Calculated diffraction spectra of the photorefractive quantum wells: (a) input diffraction efficiency; (b) and diffraction phase. The diffraction efficiency is calculated using both the transmission spectrum and electro-optic effect. The phase is only calculated from the electro-optic effect. Note that the phase is flat near 850 nm.

The femtosecond pulse is diffracted from the photorefractive quantum well using non-degenerate four-wave mixing, as shown in Fig. 1. The femtosecond pulse source is a Clark NJA-4 modelocked Ti-Sapphire laser (with 100 MHz repetition rate), pumped by a Coherent Innova-310 Argon Ion laser. A 685 nm diode laser is the source for the writing beams, with a photon energy above the bandgap of the quantum well barriers. The fringe spacing of the interference pattern is 10 μm , which is far above the resolution limit of 3 μm and below the limit where scattered light from the transmitted beam overlaps with the diffraction. The incident intensity from the writing beams is 2 mW total with a beam ratio of unity, while there is 2 mW in the probe pulsed beam, which results in a total intensity of approximately 40 mW/cm². To obtain the largest diffraction efficiency, the writing beams should be much stronger than the probe, but diffracted power is maximized when the ratio of the writing beam power to the probe power is near unity. An advantage of photorefractive quantum wells is their ultra-low sensitivity, where the gratings are fully developed for a saturation intensity of 10 $\mu\text{W}/\text{cm}^2$. There is a trade-off between response time and intensity, with shorter response times for higher intensities. At an intensity of 40 mW/cm², the response time is about 10 μs . Over the duration of one 100 fs pulse, the photorefractive grating remains essentially static. To obtain diffraction, a field is applied by applying 400V DC over a 1 mm gap for an average field of 4 kV/cm, and the writing beams are chopped at 1.0 kHz.

The shape of the pulse is measured using the linear techniques described above, which use an undistorted reference pulse. The delay line for the reference pulse uses a hollow retroreflector mounted on a stepper-motor driven translation stage with a 0.1 μm step size. A biased p-i-n silicon photodetector is used for electric-field correlation. Spectra are measured with a 0.275 m spectrometer with a CCD for capture. Nonlinear correlation is accomplished with 0.5 mm thick BBO with a photomultiplier tube to detect the second harmonic. Both field and second-harmonic correlation scans are performed by chopping the writing beams and measuring the signal with a lockin amplifier. For correlation scans, the envelope function can be used to estimate the signal pulse shape, given the properties of the reference pulse. However, the combination of the uncertainty of the translation stage and drift of the relative path lengths as the translation stage is scanned makes phase information unreliable for correlation scans. There is no drift between adjacent points in the spectra because the CCD captures all points simultaneously.

V. Data and Analysis

The characteristics of the reference pulse are important for interferometric and correlation techniques. Pulses from the laser used in this experiment are typically 100 fs in duration and are nearly transform limited gaussian pulses. The reference pulse electric field autocorrelation is shown in Fig. 4(a), and the interferometric second harmonic autocorrelation is shown in Fig. 4(b). The sign convention is that positive delays correspond to the reference pulse arriving after the signal pulse at the detector. Therefore, the leading edge of the pulse is on the left, so the pulse appears to be moving from right to left. With a 100 nm step size for the translation stage and approximately 850 nm center frequency, there are over four points per interference fringe. The heavy line in Fig. 4(a) is the envelope of the correlation function $\gamma_{R,R}(\tau)$ calculated using Eq. 30, which has a width of 213 fs. The power spectrum is shown in Fig. 5(a) with a width of 8.8 nm, and the average of the second harmonic autocorrelation is shown in Fig. 5(b) with a width 158 fs. Both curves in Fig. 5 are fitted with gaussian functions to show that the pulse is approximately a gaussian shape. Electric field autocorrelation of the reference and the Fourier transform of the spectrum match well, as shown in Fig. 6. These curves should match according to Eq. 26, which verifies that the spectral data is consistent with the correlation data. The time-bandwidth product is calculated directly from the spectrum

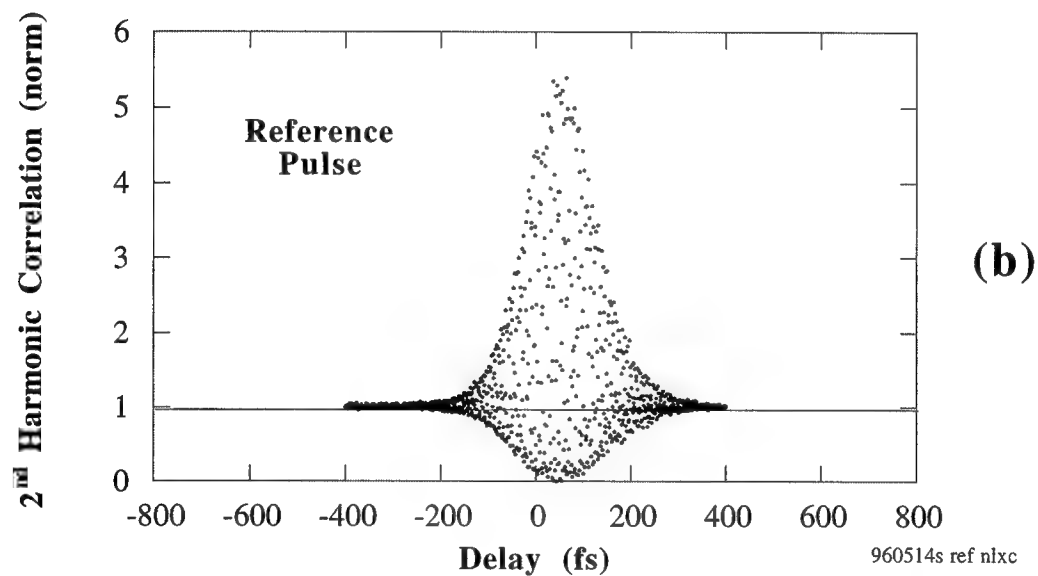
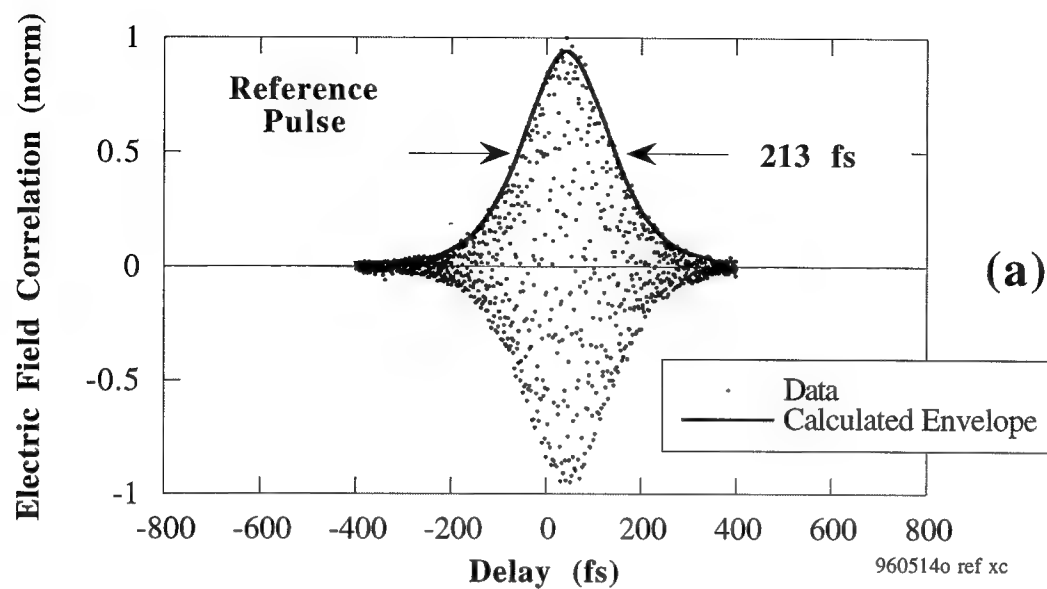


Fig. 4. Reference pulse auto-correlation vs. delay: (a) electric field auto-correlation of reference pulse; (b) interferometric second harmonic autocorrelation of reference pulse. In (a), the heavy line is the calculated envelope.

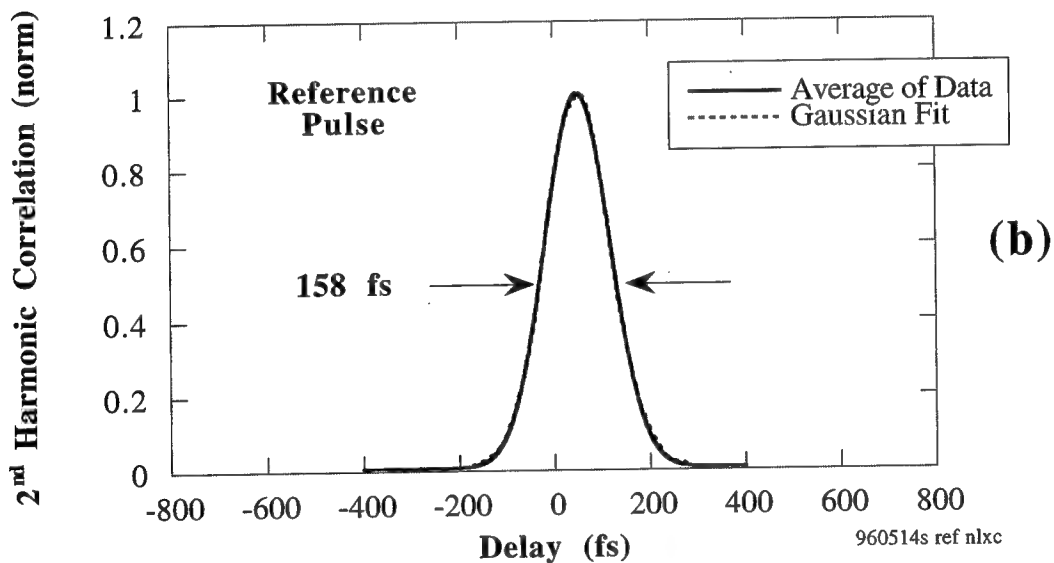
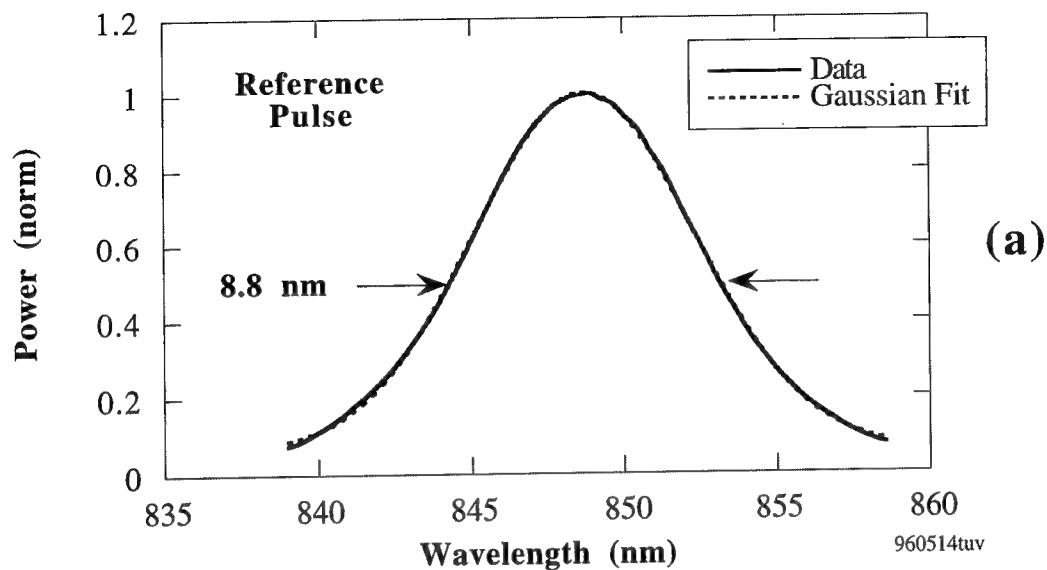


Fig. 5. Gaussian fits to reference pulse: (a) gaussian fit to reference pulse spectrum; (b) gaussian fit to reference pulse second harmonic autocorrelation, which is the average of the data in Fig. 4(b). Both curves are well fit by a gaussian. The reference pulse is nearly transform limited.

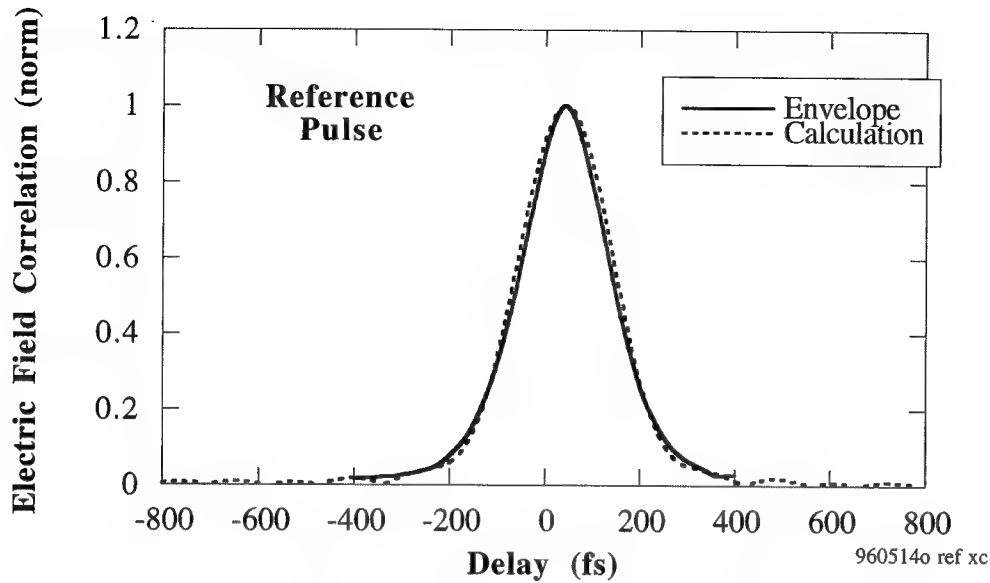


Fig. 6. Electric field autocorrelation of reference pulse and inverse Fourier transform of reference pulse power spectrum. The agreement between the two curves indicates consistency between the correlation and spectral measurements.

using $t_p v = t_p c \Delta\lambda / \lambda^2$, where $c = 300$ nm/fs, and t_p is calculated from the second harmonic autocorrelation width using Eq. 30. The time-bandwidth product for the reference pulse is 0.41, which is consistent with a transform limited gaussian pulse.

The absorption and refractive index spectra distort the transmitted pulse. The electric field cross-correlation of the transmitted and reference pulses is shown in Fig. 7(a), and the interferometric cross-correlation is shown in Fig. 7(b). The transmitted pulse has a tail on the following edge of the pulse. The power spectrum in is shown in Fig. 8(a) and the phase spectrum is shown in Fig. 8(b), calculated from the spectral interference of the transmitted pulse with the reference pulse. The tail is due to either the amplitude or phase of the transmission function $H_T(\omega)$. In Fig. 9, the power spectrum data is compared with the power spectrum calculated from the product of the transmission in Fig. 2(a) and from the power spectrum of the reference pulse. In Fig. 10, the electric-field cross-correlation data is compared with calculations from spectral measurements. The calculation using both the amplitude and the phase nearly matches the data, while the calculation without the phase fails to produce a tail. Therefore, photorefractive quantum wells distort transmitted pulses due to both absorption and refractive index variation over the bandwidth of the pulse.

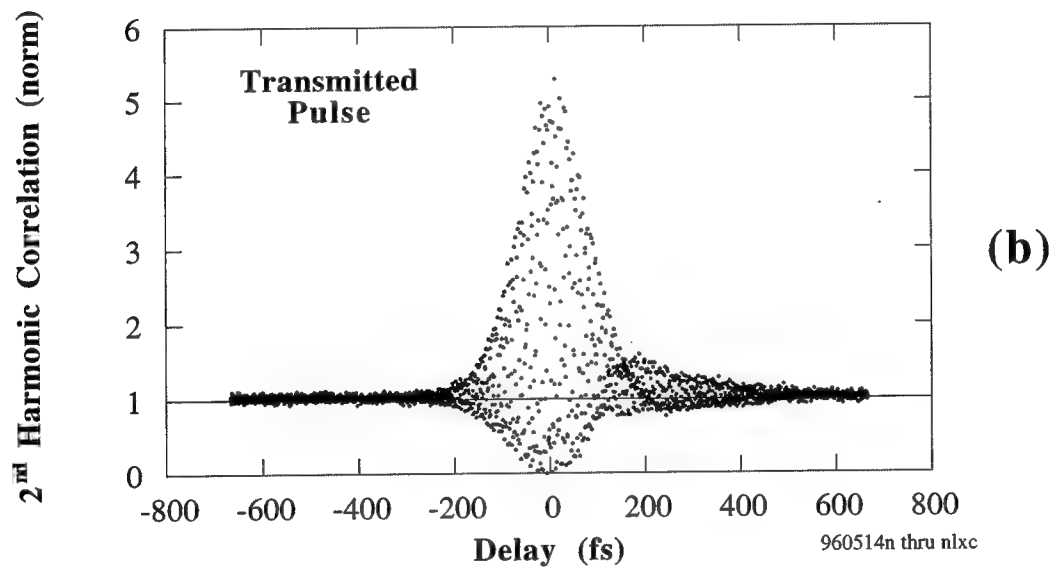
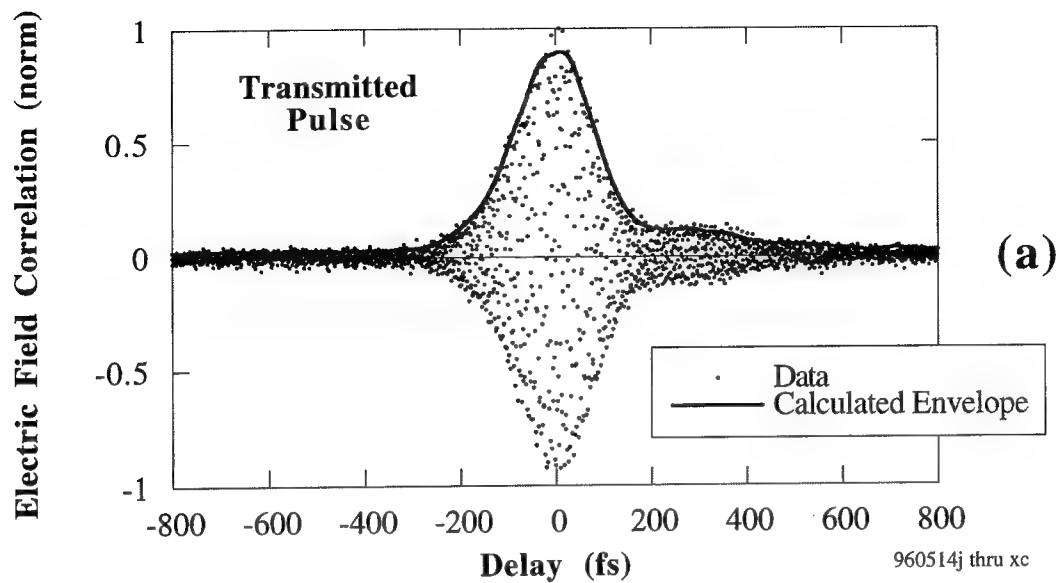


Fig. 7. Cross-correlation of transmitted pulse with reference pulse vs. reference pulse delay: (a) electric field cross-correlation; (b) interferometric second harmonic cross-correlation. The transmitted pulse shape has gained a tail on the following edge of the pulse.

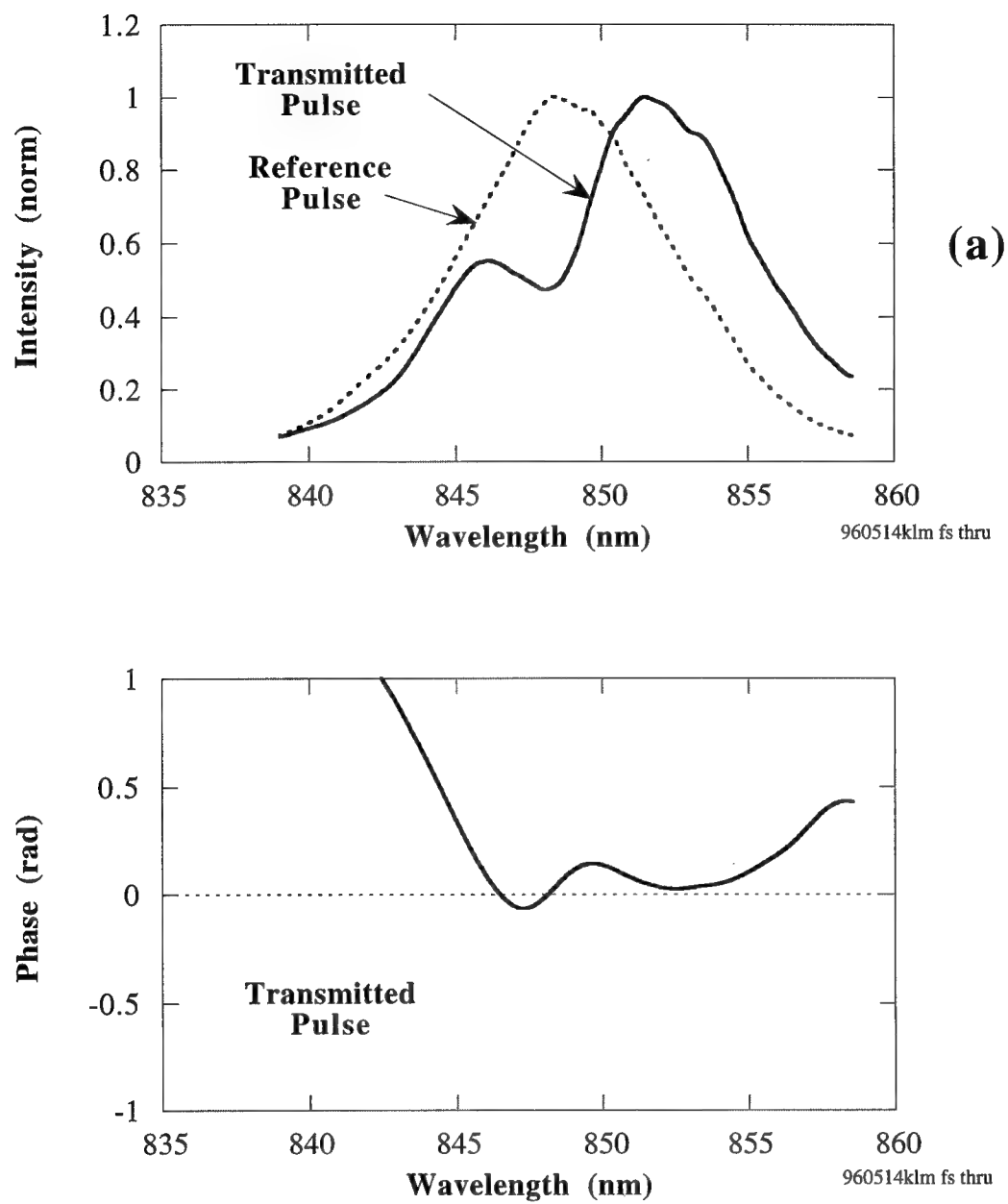


Fig. 8. Spectrum of transmitted pulse: (a) transmitted and reference pulse spectra; (b) transmitted pulse phase measured by spectral interference. There is a notch in the transmitted pulse spectrum due to the heavy hole exciton absorption feature.

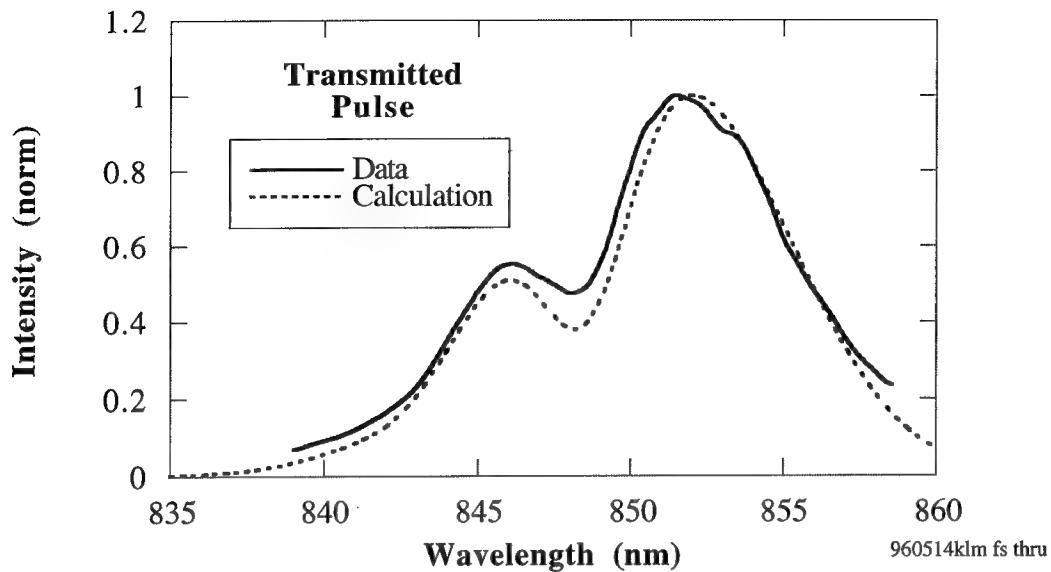


Fig. 9. Spectrum of transmitted pulse and calculated spectrum.

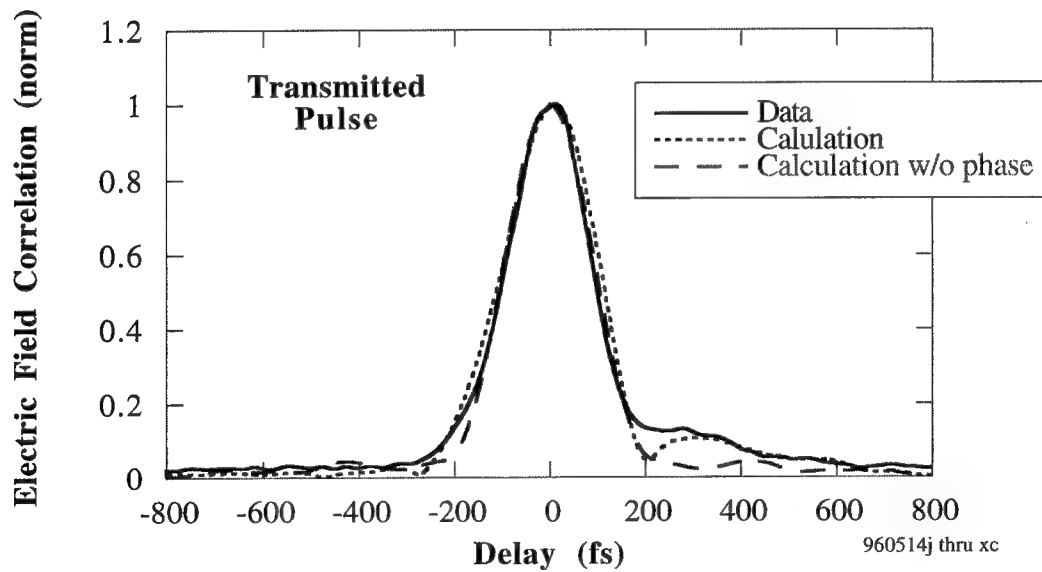


Fig. 10. Electric field cross-correlation of transmitted pulse. The first calculation uses the amplitude and phase from the spectral measurements, while the second calculation uses only the amplitude, with the phase set to zero. The phase is necessary to describe the tail on the correlation.

The peak of the diffraction efficiency spectrum in Fig. 3(a) broadens the diffracted pulse by reducing its bandwidth. The electric-field cross-correlation of the diffracted and reference pulses is shown in Fig. 11. The calculated envelope has a width of 433 fs, more than twice as long as the reference field autocorrelation width of 213 fs. Assuming the diffracted pulse is a transform limited gaussian, Eq. 24 can be used to estimate that the diffracted pulse duration is

$$t_S = \sqrt{\frac{\tau_{S,R}^2}{2} - t_R^2} \quad (38)$$

which is 285 fs, where the reference pulse duration is the same as used above. The increased duration of the diffracted pulse compared to the reference pulse is in general due to a combination of the decreased bandwidth of the pulse, and the variation of the refractive index over the bandwidth, that is, chirping (or higher order) changes in the phase. In Fig. 12(a), the spectra of the reference and diffracted pulse are shown. The diffraction spectrum appears to also be nearly gaussian, and the spectrum and the estimate of the pulse length are used to calculate a time-bandwidth product of 0.43, also very close the that for a gaussian. The phase in Fig. 12(b) is nearly flat, confirming that the pulse is nearly transform limited.

The spectrum of the diffracted pulse is calculated from the electro-optic data and compared with the data in Fig. 13. The difference between the data and the calculation is likely due to the difference between the modulation depth of the space-charge field during photorefractive mixing and the modulation of the field used for differential transmission. Even with a beam ratio of unity in the writing beams, the effective modulation of the space-charge field will be limited by the transport. If the effective space-charge modulation were known, then a precise comparison could be made. Some error may also be due to nonuniform distribution of the field between the contacts [23], but this effect should be small since the incident intensity is high.

The electric-field correlation of the diffracted and reference pulses is calculated from the spectral data using Eq. 18 and compared with the data in Fig. 14. The calculation with and without the phase are nearly identical, indicating that the phase variation of the diffracted pulse is small, so the pulse is nearly transform limited.

In conclusion, pulses diffracted from photorefractive quantum wells are broadened, but remain nearly transform limited. The broadening is due to the bandwidth of the diffraction efficiency spectrum, which is determined by the electro-optic properties of the quantum wells. Since the phase of the diffracted pulses remain essentially flat, therefore, the chief limitation to the diffracted pulsewidth is the photorefractive bandwidth, not the dispersion of the index gratings. This indicates that photorefractive quantum well devices will be useful for pulse shaping. Future work includes the design of structures with wider bandwidth through bandgap engineering of the quantum well structure [24]. To obtain more diffracted power, asymmetric Fabry-Perot structures [25], and perpendicular geometry p-i-n structures [26] are being explored. Finally, photorefractive materials that operate at a wavelength of 1.5 μm [27] are required for pulse shaping compatible with fiber-optic communications technology.

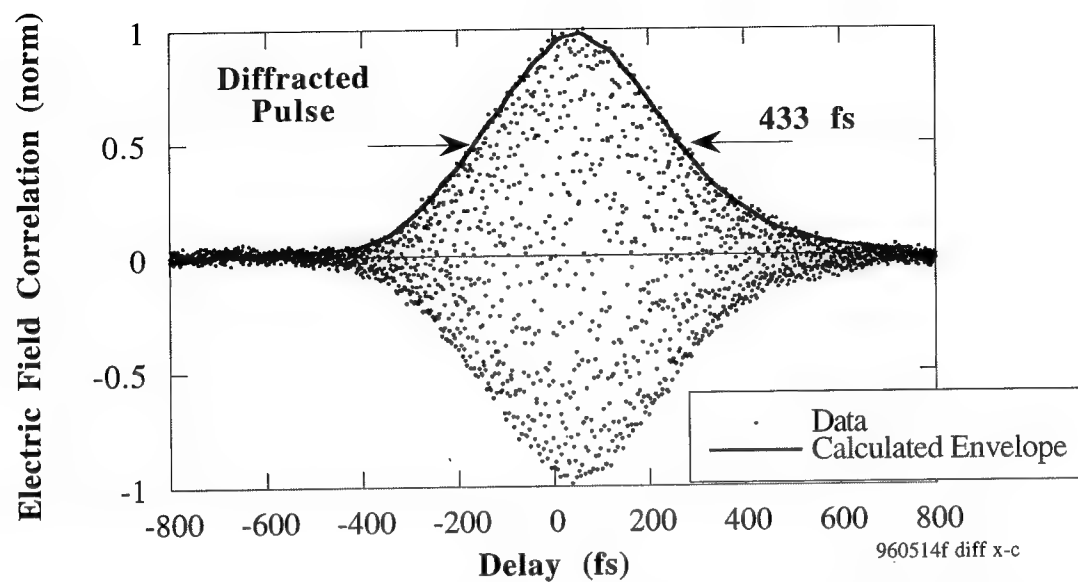


Fig. 11. Electric field cross-correlation of the diffracted pulse and the reference pulse. The diffracted pulse is estimated to be 2.5 times longer than the reference pulse.

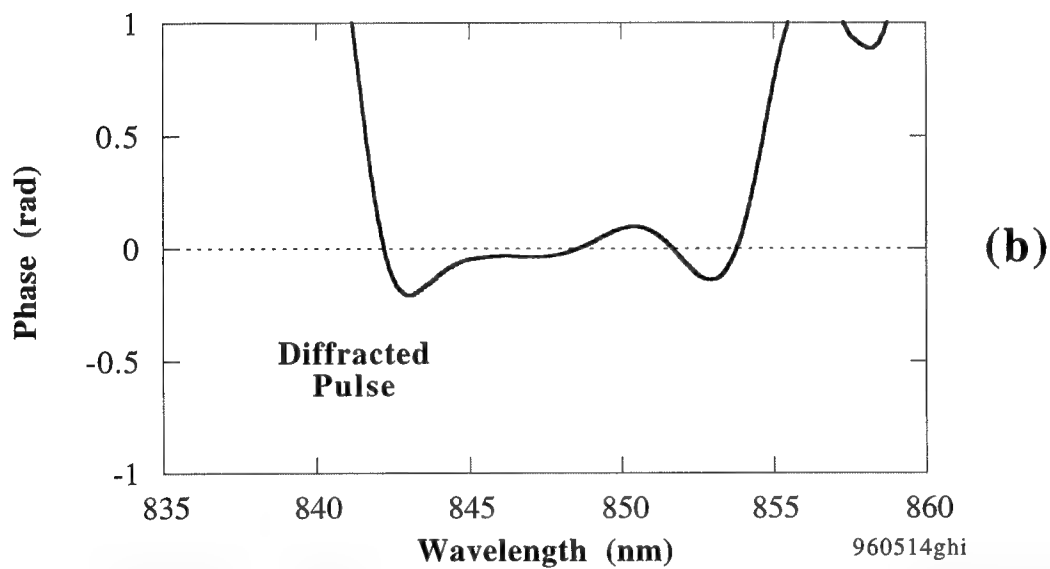
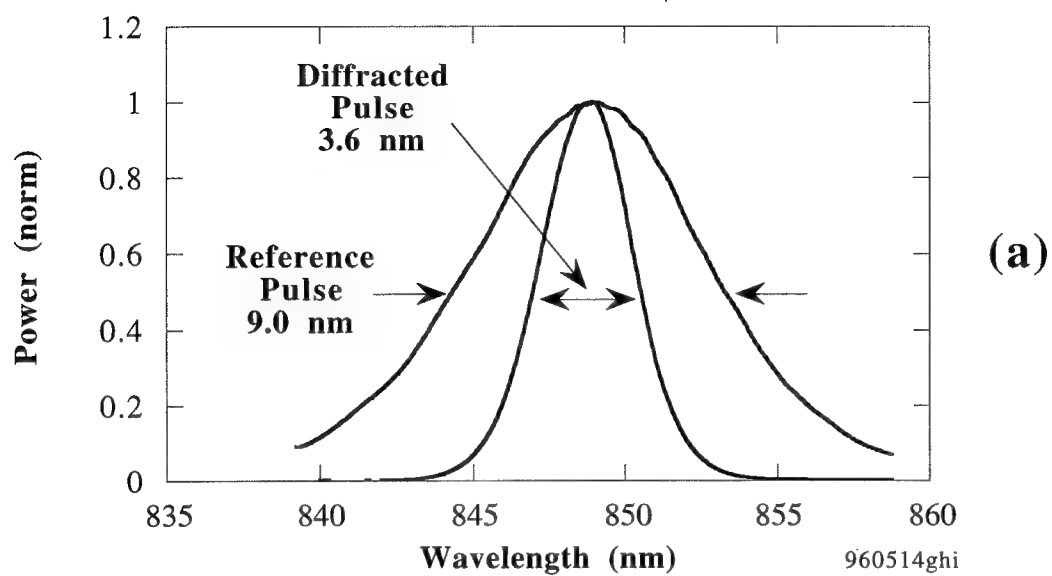


Fig. 12. Spectra of the diffracted pulse: (a) power spectrum of the diffracted pulse compared to reference pulse; (b) phase of the diffracted pulse. The diffracted pulse is also nearly a gaussian shape.

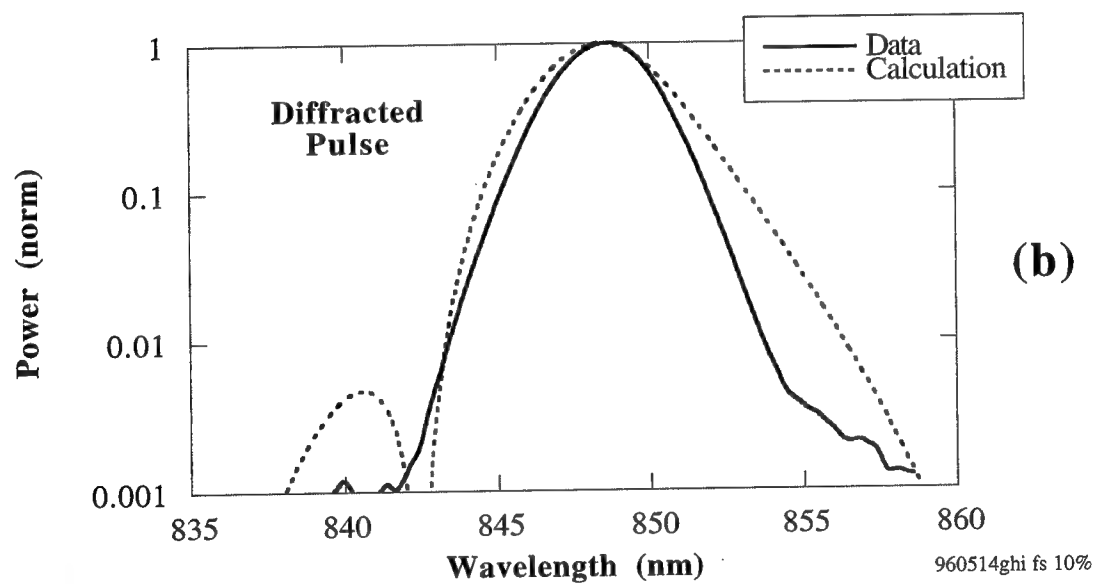
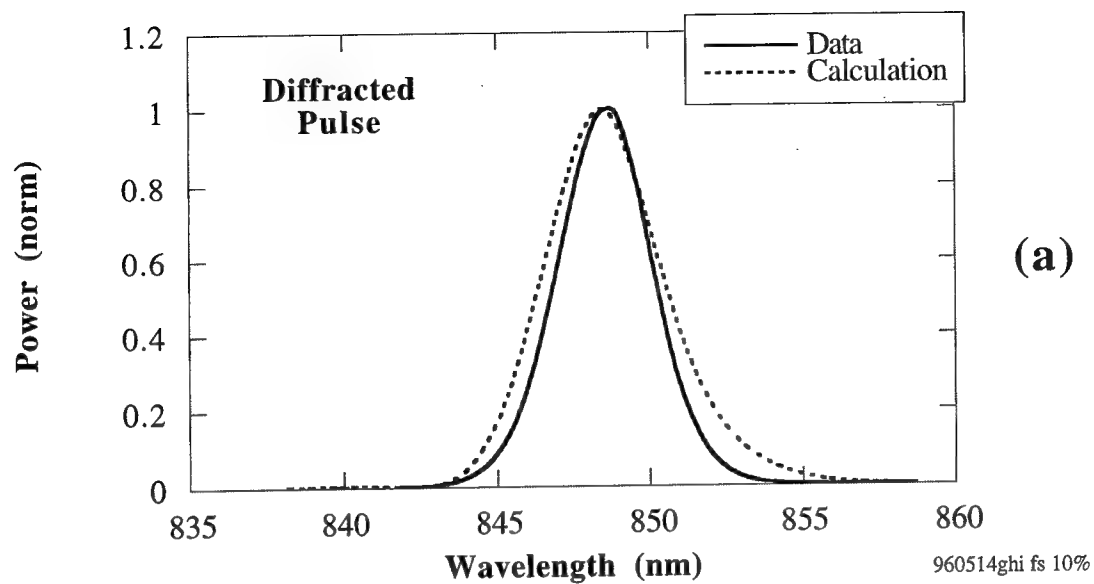


Fig. 13. Spectrum of the diffracted compared with calculation from transmission and electro-optic data: (a) linear scale; (b) log scale.

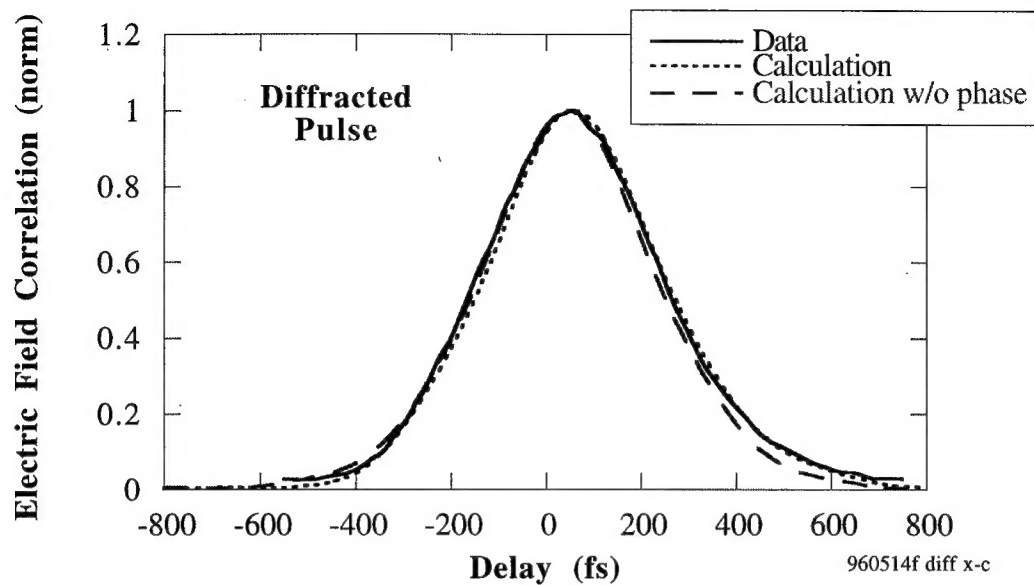


Fig.14. Electric-field cross correlation of diffracted pulse with reference pulse. The calculation is from spectral data. The small difference between the calculation with and without phase indicates the pulse is nearly transform limited.

VI. References

1. A. M. Weiner, "Femtosecond Optical Pulse Shaping and Processing," *Prog. Quant. Electr.* **19**, 161 (1995).
2. A. M. Weiner, J. P. Heritage, and E. M. Kirschner, "High-resolution femtosecond pulse shaping," *J. Opt. Soc. Am. B* **5** (8), 1563 (1988).
3. Andrew M. Weiner, Daniel E. Leaird, J. S. Patel, and John R. Wullert, II, "Programmable Shaping of Femtosecond Optical Pulses by Use of 128-Element Liquid Crystal Phase Modulator," *IEEE J. Quantum Electron.* **28** (4), 908 (1992).
4. Marc M. Wefers and Keith A. Nelson, "Programmable phase and amplitude femtosecond pulse shaping," *Opt. Lett.* **18** (23), 2032 (1993).
5. Andrew M. Weiner, Daniel E. Leaird, David H. Reitze, and Eung Gi Paek, "Femtosecond spectral holography," *IEEE J. Quantum Electron.* **28** (10), 2251 (1992).
6. D. D. Nolte and M. R. Melloch, "Photorefractive Quantum Wells and Thin Films," in *Photorefractive Effects and Materials*, edited by D. D. Nolte (Kluwer Academic Publishers, Dordrecht, 1995).
7. Q. N. Wang, R. M. Brubaker, D. D. Nolte, and M. R. Melloch, "Photorefractive Quantum Wells: Transverse Franz-Keldysh Geometry," *J. Opt. Soc. Am. B* **9**, 1626 (1992).
8. Rick Trebino, Carl C. Hayden, Anthony M. Johnson, Wayne M. Simpson, and Alfred M. Levine, "Chirp and self-phase modulation in induced-grating autocorrelation measurements of ultrashort pulses," *Opt. Lett.* **15** (19), 1079 (1990).
9. Vince Dominic, X. Steve Yao, R. M. Pierce, and Jack Feinberg, "Measuring the coherence length of mode-locked laser pulses in real time," *Appl. Phys. Lett.* **56** (6), 521 (1990).
10. L. H. Acioli, M. Ulman, E. P. Ippen, J. G. Fujimoto, H. Kong, B. S. Chen, and M. Cronin-Golomb, "Femtosecond temporal encoding in barium titanate," *Opt. Lett.* **16** (24), 1984 (1991).
11. X. Steve Yao, Vince Dominic, and Jack Feinberg, "Theory of beam coupling and pulse shaping of mode-locked laser pulses in a photorefractive crystal," *J. Opt. Soc. Am. B* **7** (12), 2347 (1990).
12. R. M. Brubaker, Q. N. Wang, D. D. Nolte, E. S. Harmon, and M. R. Melloch, "Steady-state four-wave mixing in photorefractive quantum wells with femtosecond pulses," *J. Opt. Soc. Am. B* **11** (6), 1038 (1994).
13. Martin C. Nuss, Melissa Li, T. H. Chiu, A. M. Weiner, and Afshin Partovi, "Time-to-space mapping of femtosecond pulses," *Opt. Lett.* **19** (9), 664 (1994).
14. Q. N. Wang, D. D. Nolte, and M. R. Melloch, "Spatial-harmonic gratings at high modulation depths in photorefractive quantum wells," *Opt. Lett.* **16** (24), 1944 (1991).
15. X. D. Cao and D. D. Meyerhofer, "Frequency-domain interferometer for measurement of the polarization mode dispersion in single-mode optical fibers," *Opt. Lett.* **19** (22), 1837 (1994).

16. L. Lepetit, G. Chériaux, and M. Joffre, "Linear techniques of phase measurement by femtosecond spectral interferometry for applications in spectroscopy," *J. Opt. Soc. Am. B* **12** (12), 2467 (1995).
17. Rick Trebino and Daniel J. Kane, "Using phase retrieval to measure the intensity and phase of ultrashort pulses: frequency-resolved optical gating," *J. Opt. Soc. Am. A* **10** (5), 1101 (1993).
18. Y. Silberberg, P. W. Smith, D. A. B. Miller, B. Tell, A. C. Gossard, and W. Wiegmann, "Fast nonlinear optical response from proton-bombarded multiple quantum well structures," *Appl. Phys. Lett.* **46**, 701 (1985).
19. Donald C. D'Avanzo, "Proton Isolation for GaAs Integrated Circuits," *IEEE Trans. Electron Devices* **ED-29** (7), 1051 (1982).
20. P. Günter and J.-P. Huignard, "Photorefractive Materials and Their Applications I and II," in *Topics in Applied Physics* (Springer-Verlag, Berlin, 1988), Vol. 61.
21. Ralph Williams, *Modern GaAs Processing Methods* (Artech House, Boston, 1990).
22. E. Yablonovitch, T. Gmitter, J. P. Harbison, and R. Bhat, "Extreme selectivity in the lift-off of epitaxial GaAs films," *Appl. Phys. Lett.* **51**, 2222 (1987).
23. D. D. Nolte, N. P. Chen, M. R. Melloch, C. Montemagno, and N. M. Haegel, "Electroabsorption field imaging between coplanar metal contacts on semi-insulating semiconductor epilayers," *Appl. Phys. Lett.* **68** (1), 72 (1996).
24. Mihaela Dinu, M. R. Melloch, and D. D. Nolte, "Electro-optic and photorefractive properties of long-period Fibonacci superlattices," *J. Appl. Phys.* **79** (7), 3787 (1996).
25. K. M. Kwolek, M. R. Melloch, D. D. Nolte, and G. A. Brost, "Photorefractive asymmetric Fabry-Pérot quantum wells: Transverse-field geometry," *Appl. Phys. Lett.* **67** (6), 736 (1995).
26. I. Lahiri, María Aguilar, D. D. Nolte, and M. R. Melloch, "High-efficiency Stark-geometry photorefractive quantum wells with intrinsic cladding layers," *Appl. Phys. Lett.* **68** (4), 517 (1996).
27. C. De Matos, A. Le Corre, H. L'Haridon, B. Lambert, S. Salaün, J. Pleumeekers, and S. Gosselin, "Photorefractive p-i-n diode quantum well operating at 1.55 μm ," *Appl. Phys. Lett.* **68** (25), 3576 (1996).

MISSION OF ROME LABORATORY

Mission. The mission of Rome Laboratory is to advance the science and technologies of command, control, communications and intelligence and to transition them into systems to meet customer needs. To achieve this, Rome Lab:

- a. Conducts vigorous research, development and test programs in all applicable technologies;
- b. Transitions technology to current and future systems to improve operational capability, readiness, and supportability;
- c. Provides a full range of technical support to Air Force Material Command product centers and other Air Force organizations;
- d. Promotes transfer of technology to the private sector;
- e. Maintains leading edge technological expertise in the areas of surveillance, communications, command and control, intelligence, reliability science, electro-magnetic technology, photonics, signal processing, and computational science.

The thrust areas of technical competence include: Surveillance, Communications, Command and Control, Intelligence, Signal Processing, Computer Science and Technology, Electromagnetic Technology, Photonics and Reliability Sciences.